Research Article Wiley Online Library ELECTROANALYSIS

doi.org/10.1002/elan.202200102

Practical Insights into the Impedance Response of Interdigitated Electrodes: Extraction of Relative Static Permittivity and Electrolytic Conductivity

Benedikt Sapotta,[a] Matthias Schwotzer,[a] and Matthias Franzreb*[a]

Abstract: This work aims to provide a detailed understanding of the challenges related to the computation of the relative static permittivity and electrolytic conductivity of a sample medium from its impedance response recorded with interdigitated electrode (IDE) geometries. Within the scope of the study, impedance data has been measured and evaluated for a total of nine sample media using two distinct IDE geometries. Particular emphasis is laid upon the compensation of parasitic influences affecting the impedance response. With the raw data supporting this study fully disclosed, the reader is offered the opportunity to comprehensively retrace the evaluation procedure proposed in the text.

Keywords: impedance spectroscopy · dielectric spectroscopy · interdigitated electrodes · conductivity · permittivity

1 Introduction

Thin film interdigitated electrodes (IDEs) are comprised of two planar, interlaced comb structures of a conductive material deposited on a dielectric substrate. IDEs can be produced at low-cost in great numbers owing to sophisticated microfabrication techniques and as such have gained increasing popularity for a variety of applications [1]. The IDE geometry is usually realized as a disposable electrode chip, a model of which is displayed in Figure 1.

As the standardized IDE structure is capable of providing conclusive current signals even for highly resistive sample media under test (SUTs), it is particularly attractive for impedimetric applications. For this reason, the IDE geometry is frequently employed to track minor variations to bulk properties of SUTs in contact with the interdigitated area, most notably its electrolytic conductivity κ_{SUT} and relative permittivity $\varepsilon_{r,SUT}$. Accordingly, IDEs have been repeatedly employed for the impedance based detection of water content in a variety of different SUTs ranging from organic liquids [2] to soil samples [3] as well as building materials [4] and the human skin [5]. On a fundamental level, impedimetric moisture sensing applications rely by and large on the increase of $\varepsilon_{r,SUT}$ upon uptake of water molecules into the respective SUT. On the other hand, IDE chips are often coated with a sensitive material which can then be used for chemocapacitive [6] or alternatively for chemiresistive [7] gas sensing; again owing to variations in $\varepsilon_{r,SUT}$ or κ_{SUT} upon sorption of target molecules into the sensitive layer under test. When applied as electroanalytic technique, the measurement of κ_{SUT} and $\varepsilon_{r,SUT}$ is referred to as *conductometry* and *dielectrometry*, respectively [8]. Interdigitated conductometry is particularly attractive in biosensing [9] due to the low sample volume requirements and ease of chemical functionalisation. Interdigitated dielectrometry on the other hand allows the in-situ cure monitoring of thermoset materials [10] within the framework of the more generalized dielectric (thermal) analysis approach [11]. In addition, interdigitated dielectrometry provides unique opportunities for thin film characterization [12], especially when integrated into an overarching impedance spectrum analysis [13].

Any target-oriented realisation of the impedimetric applications mentioned above requires a conceptual

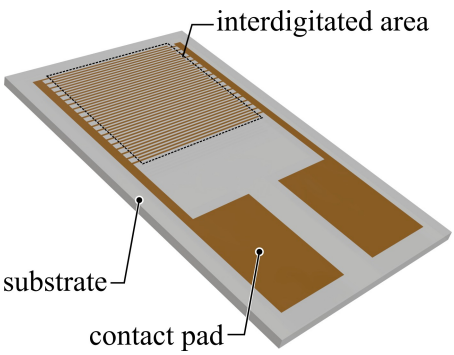

Fig. 1. Model of a customary interdigitated electrode chip comprised of two interlaced conductive comb structures deposited on a dielectric substrate. The sample medium under test is placed onto the interdigitated area for impedimetric analysis.

[a] B. Sapotta, M. Schwotzer, M. Franzreb
Institute of Functional Interfaces (IFG), Karlsruhe Institute of Technology (KIT), Eggenstein-Leopoldshafen, Karlsruhe, 76344, Germany
E-mail: matthias.franzreb@kit.edu

Supporting information for this article is available on the WWW under https://doi.org/10.1002/elan.202200102

understanding of how the underlying bulk properties enter the measured impedance data, particularly in relation to a variety of confounding effects. Especially if absolute values of rather than just relative change to κ_{SUT} or $\varepsilon_{r,SUT}$ are of interest, the peculiarities of the IDE geometry deserve special attention. For instance, recent studies on the impedance response of IDEs suggest considerable influence of geometry-induced frequency dispersion owing to the inherent inhomogeneity of the potential and current distributions [14]. In addition, IDE chips impart characteristic parasitic contributions to the impedance response which when left unaccounted for, might lead to a misinterpretation of the data.

The purpose of this work is to substantiate how and to what degree reliable κ_{SUT} and $\varepsilon_{r,SUT}$ values can be obtained with IDE structures. To this end, we recorded the impedance response of a total of nine different SUTs. With both dielectric and conductivity reference media among the sample media examined, the recorded IDE impedance data sets are comprehensively tested against the common theory of κ_{SUT} and $\varepsilon_{r,SUT}$ extraction. To support the general validity of the findings, the impedance spectra were taken with two different IDE geometries.

2 Theoretical Framework for Obtaining Relative Static Permittivity and Electrolytic Conductivity

This chapter summarizes a few conceptual steps that need to be considered when trying to determine the bulk dielectric and conductive properties of a homogeneous sample medium by impedance spectroscopy. While the primary focus is laid on the interdigitated electrode structure, similar considerations are required irrespective of the particular electrode geometry used.

In order to extract κ_{SUT} and $\varepsilon_{r,SUT}$ values from the impedance data, the respective material properties are assumed isotropic as well as adequately invariant to the local electric field strength and AC frequency applied. Isotropy is reasonably justified for most fluidic sample media. E-field dependence on the other hand is usually expected at field strengths exceeding several MV/m [15], which however will only become relevant under specialized experimental conditions. While frequency dependence of κ_{SUT} is considered insignificant [16], $\varepsilon_{r,SUT}$ in general needs to be treated as a complex function of the frequency. The permittivity can however be considered as a real and sufficiently frequency-invariant quantity at "low" frequencies [17]. The static relative permittivity assumption has been suggested to be reasonably applicable at frequencies of 1 MHz and below for a variety of liquids [18].

2.1 Differentiation of Measured Impedance Response into Parasitic and Sample Medium Contributions

When recording an impedance spectrum, it is important to acknowledge that the measured impedance response $\boldsymbol{Z_M}$ is not necessarily equivalent to the impedance response $\boldsymbol{Z_{SUT}}$ exerted by the sample medium under test (SUT) in contact with the designated electrode structure. In addition to $\boldsymbol{Z_{SUT}}$, $\boldsymbol{Z_M}$ may also be affected by parasitic contributions stemming from the electrical integration of the electrode structure into the impedance measurement system.

In general, impedimetric measurement setups should be carefully designed to minimize any parasitic contributions e.g. by optimizing the length and placement of the leads connecting the electrode structure with the impedance measurement hardware. If the experimental system is purposefully designed and the measurement conducted at frequencies for which parasitic contributions are negligible, practical equality of $\boldsymbol{Z_{SUT}}$ and $\boldsymbol{Z_M}$ is often assumed. This approach however is not reasonable when trying to obtain bulk material properties with IDE geometries. One factor worth considering is the finite thickness of the conductive material the electrode structure is composed of. For example, with commonly encountered metal film thicknesses of a few hundreds of nanometers or below [14b,19], the real part of the impedance measured for a highly conductive sample medium might be limited by the current flow between contact pad and interdigitated area or even within the electrode fingers themselves. On the other hand, the electric field surrounding the counter charged electrode fingers not only penetrates the sample space above the interdigitated area but also the electrode substrate onto with the electrode structure is deposited. For this reason, a parasitic geometric capacitance related to the actual electrode substrate will always be present in parallel to $\boldsymbol{Z_{SUT}}$ in $\boldsymbol{Z_M}$.

When considered significant and unavoidable, parasitic contributions to $\boldsymbol{Z_M}$ need to be actively compensated for. There are a variety of practical strategies for this purpose [20].

The approach pursued in this work is to capture the individual parasitic contributions into lumped elements put together into an equivalent circuit model. In this regard, special attention is given to the electron conducting leads connecting the interdigitated area to the impedance analyser imparting a serial parasitic resistance $\boldsymbol{R_P}$ and inductance $\boldsymbol{L_P}$. In addition, a geometric capacitance $\boldsymbol{C_{Geo,P}}$ in parallel is considered due to e.g. proximity of the electron conducting segments. A leakage resistance effectively bypassing $\boldsymbol{Z_{SUT}}$ is not specifically accounted for in this study but might become relevant for high impedance SUTs at low frequencies.

In Figure 2, the parasitic components $\boldsymbol{R_P}$, $\boldsymbol{L_P}$ and $\boldsymbol{C_{Geo,P}}$ are broken down into the individual contributions of A) the electrical integration of the electrode chip into the measurement system and B) the electrode chip itself. This differentiation of parasitic contributions to $\boldsymbol{Z_M}$ is in general not necessary for the sole purpose of compensation. It may however prove useful to identify and potentially eliminate dominant parasitic contributors. The modelling of the parasitic impedance with the help of a lump-element model is based on the assumption, that its

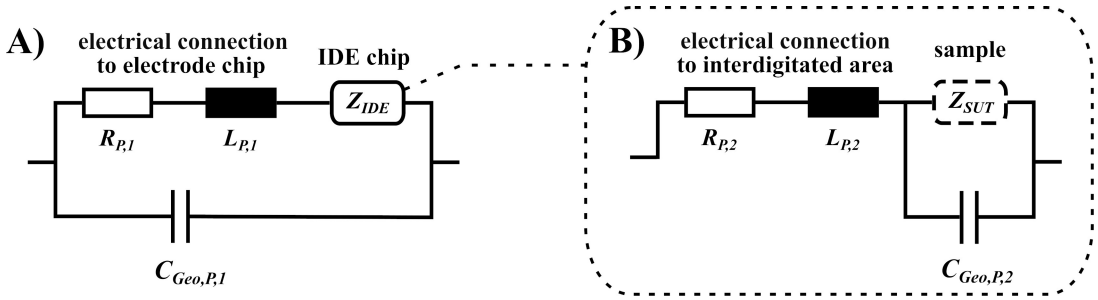

Fig. 2. Equivalent circuit models to account for parasitic influences present in the **A)** electric connection to the IDE chip and **B)** the IDE chip itself.

individual components are sufficiently stable and as such do not change significantly within the recorded frequency range. Especially at higher frequencies however, this assumption might be compromised due to skin or proximity effects [21].

2.2 Differentiation of Sample Medium Impedance Response into Bulk and Interfacial Contributions

Impedance spectroscopy provides information both about the bulk of the SUT as well as the interface between SUT and electrode [22]. When working with IDEs, the bulk which is stimulated by the AC current flow comprises but a thin layer of the sample medium in direct proximity with the interdigitated area whose thickness may be estimated from the electrode finger width and spacing [23]. Both ionic migration related to κ_{SUT} and dipole polarization related to $\varepsilon_{r,SUT}$ make up the bulk contribution to $\boldsymbol{Z_{SUT}}$.

Separate from bulk effects are interfacial processes most notably the formation of the electric double layer at the electrode surface. The buildup of the electric double layer due to the migration of ionic species to and subsequent accumulation at the interface between SUT and electrode continuously deprives the bulk from the actual potential gradient, a phenomenon which is also referred to as *electrode polarization* [24]. For this reason, interfacial processes become the dominant contributor to $\boldsymbol{Z_{SUT}}$ at "low" frequencies.

As in the previous section concerning the parasitic contributions, there are two principal strategies of how to gain access to the desired bulk effects from $\boldsymbol{Z_{SUT}}$, namely

i) restrict the analysis to sufficiently "large" frequencies for which interfacial contributions are negligible thereby equating $\boldsymbol{Z_{SUT}}$ with the bulk contribution and
ii) actively compensate the interfacial contribution from $\boldsymbol{Z_{SUT}}$.

While approach i) provides a more accurate picture on the bulk contributions than approach ii), the frequency range for which interfacial contributions become relevant can only be roughly estimated. In general, the larger sample medium conductivity the more quickly the ionic double layers develop i.e. interfacial effects become relevant at ever larger frequencies. Furthermore, the influence of the double layer effect on the total impedance response increases to larger frequencies when decreasing the electrode separation distance [25], which is detrimental to a bulk medium analysis conducted with interdigitated microelectrode structures. As electrode polarisation is inherently tied to ionic migration, a useful point of reference when pursuing strategy i) represents the characteristic relaxation frequency f_{CR} which is a function of $\varepsilon_{r,SUT}$ and κ_{SUT} and can be expressed as

$$\boldsymbol{f_{CR}} = \frac{1}{2\pi}\frac{\boldsymbol{\kappa_{SUT}}}{\boldsymbol{\varepsilon_0\varepsilon_{r,SUT}}} \tag{1}$$

At frequencies larger than f_{CR}, displacement current is larger than ionic migration current and interfacial contributions to $\boldsymbol{Z_{SUT}}$ are usually negligible. Depending on κ_{SUT} however, frequencies exceeding f_{CR} may not always be reasonably accessible. In aqueous media with $\varepsilon_{r,SUT} =$ 80.29 at 20 °C for instance [26], an f_{CR} value of 1 MHz is already surpassed at a moderate conductivity of $\kappa_{SUT} =$ 45 µS/cm. For this reason, active compensation of interfacial contributions to $\boldsymbol{Z_{SUT}}$ is often required.

Provided that Faradaic processes are absent, the interfacial impedance may reduce to the charge/discharge of the ionic double layer which, within the framework of electric circuit analogues, is usually modelled by a constant phase element (CPE) [24].

A straightforward equivalent circuit for Z_{SUT} comprised of the geometric capacitance $C_{Geo,SUT}$ to account for the dipole polarization in the bulk, the solution resistance $R_{S,SUT}$ to account for ionic migration in the bulk and a constant phase element CPE_{DL} to model the interfacial electrode polarisation is provided in Figure 3 I). In case interfacial processes are negligible within the recorded frequency range, CPE_{DL} may be dropped leading to the circuit shown in Figure 3 II). The simplified equivalent circuits in Figure 3 on the right by contrast assume III) the absence of any relevant ionic migration processes altogether and IV) an overly large bulk conductivity of the SUT exerting no significant $R_{S,SUT}$. While $C_{Geo,SUT}$ would still act in parallel to CPE_{DL} in IV), $C_{Geo,SUT}$ is in general orders of magnitude smaller than the interfacial capacitance associated to CPE_{DL} and can therefore be safely neglected as well.

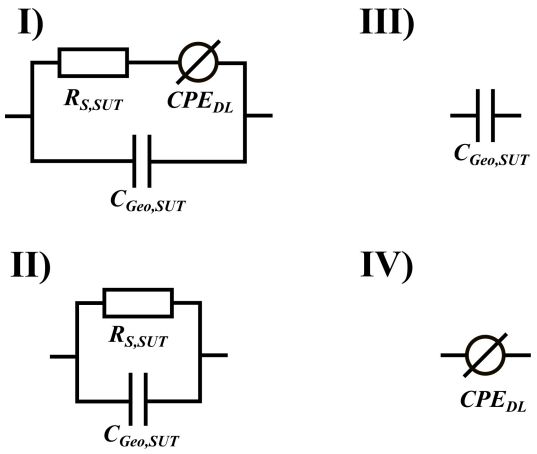

Fig. 3. I) Basic equivalent circuit model for $\boldsymbol{Z_{SUT}}$ accounting for a non-Faradaic impedance response. II)–IV) Simplifications thereof which may become reasonable depending on the frequency range or sample medium analyzed. The circuit models are used for data analysis in chapter 4.

2.3 Accessing Relative Permittivity and Electrolytic Conductivity from Equivalent Circuit Components

The magnitude of how the characteristic SUT properties $\varepsilon_{r,SUT}$ and κ_{SUT} enter Z_M depend on the electrode geometry's cell constant K_C which represents an effective ratio of electrode separation distance divided by electrode area. With ε_0 referring to the vacuum permittivity, the bulk impedance circuit components $\boldsymbol{C_{Geo,SUT}}$ and $\boldsymbol{R_{S,SUT}}$ can be converted into $\varepsilon_{r,SUT}$ and κ_{SUT} respectively via

$$\varepsilon_{r,SUT} = \frac{\boldsymbol{K_C C_{Geo,SUT}}}{\varepsilon_0} \tag{2}$$

$$\kappa_{SUT} = \frac{\boldsymbol{K_C}}{\boldsymbol{R_{S,SUT}}} \tag{3}$$

To estimate $\boldsymbol{K_C}$ of an IDE structure, analytical equations are available which require the number and length of the electrode fingers as well as the metallization ratio of the IDE structure as input parameters (see S5). Theoretically computed $\boldsymbol{K_C}$ values have been reported to underestimate the real value by usually 10–20 % [27]. The relatively poor predictability of an IDE's cell constant is said to originate from fringing effects [27] as well as geometric imperfections of an IDE structure itself [28]. Alternatively, $\boldsymbol{K_C}$ can be determined experimentally with the help of conductivity or dielectric reference media.

To summarize this chapter, the theoretical framework of how $\varepsilon_{r,SUT}$ and κ_{SUT} enter Z_M is schematically outlined in Figure 4. It is important to note that the accuracy and precision at which $\varepsilon_{r,SUT}$ and κ_{SUT} can be determined with equations (2) and (3) not only depends on the certainty at which K_C is known, but also the certainty at which the associated circuit components $\boldsymbol{C_{Geo,SUT}}$ and $\boldsymbol{R_{S,SUT}}$ can be derived from Z_M. Compensation of confounding effects is possible only up to a limited degree of certainty. Having access to a frequency range for which Z_M is exclusively dominated by the desired bulk contributions provides optimal conditions for $\varepsilon_{r,SUT}$ and κ_{SUT} extraction. In the opposite case, an impedance response whose bulk contributions are fully dwarfed by either interfacial or parasitic contributions may not reveal any quantitative information on the investigated SUT's bulk κ_{SUT} or $\varepsilon_{r,SUT}$.

Determination of $\varepsilon_{r,SUT}$ is particularly challenging in this regard as impedance contributions stemming from $\boldsymbol{C_{Geo,SUT}}$ quickly turn negligible once interfacial processes become relevant. For this reason, satisfactory mathematical compensation of electrode polarisation to gain reliable access to $\varepsilon_{r,SUT}$ is often not possible [26] and consequently measurement of $\varepsilon_{r,SUT}$ is limited to frequency ranges with insignificant interfacial impedance contribution. In case interfacial processes impart non-negligible contributions to the impedance response even at frequencies in the MHz range, the static permittivity may in fact not be accurately identifiable from the

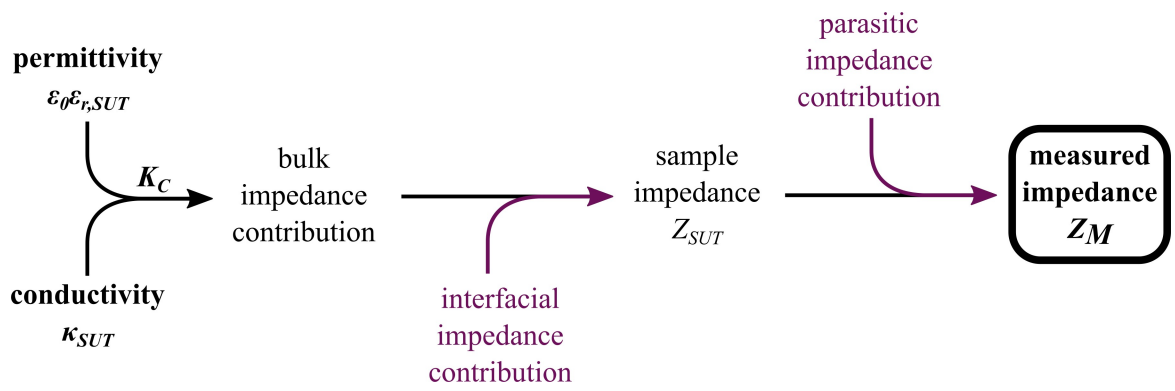

Fig. 4. Schematic flow chart outlining individual contributing effects to the measured impedance signal $\boldsymbol{Z_M}$. Both permittivity $\varepsilon_0\varepsilon_{r,SUT}$ and conductivity κ_{SUT} of a homogeneous sample medium under test (SUT) enter $\boldsymbol{Z_M}$ coupled to the electrode structure's cell constant $\boldsymbol{K_C}$ constituting the bulk impedance contribution of the respective SUT. In addition to the effects derived from the bulk of the SUT, processes occurring at the interface between SUT and electrode as well as parasitic impedance contributions are present in $\boldsymbol{Z_M}$, which need to be minimized and, if necessary, actively compensated to gain unobstructed access to the SUT's bulk properties.

impedance data at all. The static value can however still be approximated through extrapolation if a complex permittivity function of the specific SUT is available [29].

3 Outline of Experimental Approach

A detailed list of the chemicals and devices used is provided in the supporting information chapter S1 and S2.

3.1 Sample Media under Consideration

The sample media investigated in this study are specified in table 1. They were carefully chosen to test the feasibility of static relative permittivity $\varepsilon_{r,SUT}$ as well as electrolytic conductivity κ_{SUT} extraction from the impedance response of interdigitated electrodes. SUTs 1–6 serve as dielectric reference media whose static permittivity values are available in the literature. Both pure chemicals (SUTs 1–4) and mixtures (SUTs 5–6) were considered. SUTs 7–8 were commercially available conductivity reference media based on aqueous solutions of potassium chloride (KCl). A saturated solution of KCl in water roughly equivalent to 25 weight-% KCl was used as SUT 9 to, in a sense, provide a short-circuit between the electrode fingers due to its relatively large electrolytic conductivity leaving behind only parasitic and interfacial contributions to $\boldsymbol{Z_M}$.

Table 1. Sample media (SUTs) together with the recorded frequency range analysed in this study. The respective equivalent circuit models assumed for Z_{SUT} are provided in Figure 3.

No.	SUT	Freq. Range	Z_{SUT}
1	nitrogen	0.1–1 MHz	I)
2	1-butanol	0.1–1 MHz	II)
3	ethanol	0.1–1 MHz	II)
4	water	0.1–1 MHz	II)
5	ethanol/water mixture (54 mol-% ethanol)	0.1–1 MHz	II)
6	ethanol/water mixture (22 mol-% ethanol)	0.1–1 MHz	II)
7	cond. standard[a] 1410 µS/cm at 25 °C	0.005–5 MHz	III)
8	cond. standard[a] 25.0 µS/cm at 25 °C	0.005–5 MHz	III)
9	KCl saturated[a]	0.005–5 MHz	IV)

[a] in water.

3.2 Continuous Flow Setup

A microfluidic flow method was used for the impedance measurements as opposed to conventional dip or droplet based IDE chip setups due to ease of automation, inhibition of evaporation related effects and reduced risk of contamination. The experimental setup is schematically outlined in Figure 5.

A pneumatic pressure controller (operated with nitrogen gas) in conjunction with a flow selection valve allowed a sequential supply of the different sample fluids to a custom-built flow cell housing the IDE chip. The polymeric flow cell was designed in a modular configuration and prepared by 3D-printing. To guarantee chemical inertness, flow module and gasket were printed with a highly fluorinated photoresin [30]. Electrical contacting of the interdigitated electrodes was realized with pogo pins soldered to contact leads and embedded into the "connection module" located at the rear part of the flow cell. The interdigitated area of the electrodes used in this study was approximately circular in shape

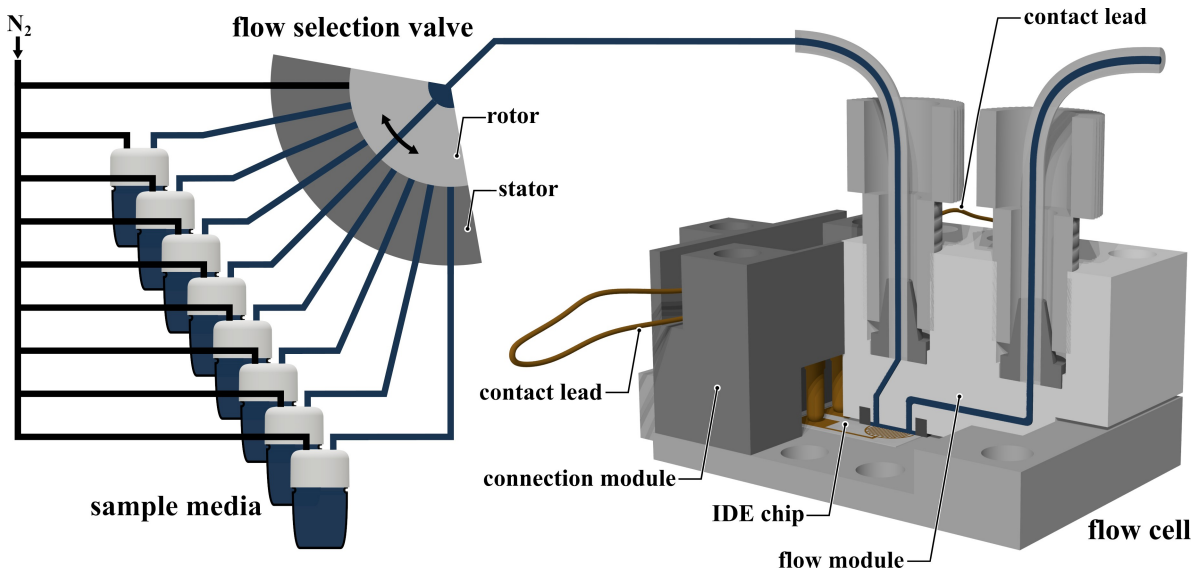

Fig. 5. Microfluidic setup used in this study. The interdigitated area of the electrode chip housed inside a modular flow cell was sequentially exposed to a total of nine sample media. The leads protruding from the connection module were contacted to a potentiostat with frequency response analyzer to measure the impedance response.

with a diameter of 3.6 mm. Inside the flow cell, the sample fluid under test was flowing through a cylindrical sensing chamber of 4 mm in diameter and 0.2 mm in height located above the interdigitated area. An initial experiment confirmed that the flow unit placed on top of the interdigitated area did not alter an impedance response taken with nitrogen as reference medium. The flow cell was operated under continuous flow conditions with a target liquid flow rate of 5 µL/s resulting in a mean liquid residence time inside the flow chamber of 0.5 seconds.

3.3 Interdigitated Electrode Chips

The IDE chips were obtained from a commercial supplier. The electrode structure was prepared of gold deposited on a glass substrate using a titanium layer as adhesion promoter. Two chips with different electrode geometries were used in this study; one with 5 µm electrode width and 5 µm spacing comprised of a total of 180 electrode pairs which within the scope of this work will be referred to as the "5 µm electrode" and one with 10 µm electrode width and 10 µm spacing comprised of a total of 90 electrode pairs which will be referred to as the "10 µm electrode" from now on. Prior to the experimentation, the IDE chips were rinsed with deionized water followed by a dry etching step using an ultraviolet-ozone surface treatment.

3.4 Recording of Impedance Spectra

Impedance spectra were taken using a potentiostat equipped with frequency response analyser. For each SUT, the voltage amplitude was optimized for Z_{SUT} to be recorded within a single current measurement range of the potentiostat, a full list of the voltage amplitudes applied is provided in S3. To verify reproducibility as well as stationarity of the measurements, a total of three consecutive impedance spectra at 40 frequency points per decade were taken for each SUT. A custom written python script allowed full automation of the measurement system. During operation of the measurement script, the system was left undisturbed to avoid interference with triboelectric phenomena or subtle changes to the capacitive coupling of the electrical connection to the environment.

The parasitic contributions of the cabling connecting the IDE chip with the potentiostat (cell cable + flow cell connection module) were determined prior to the experimentation. For this purpose, the flow cell was connected to the potentiostat and impedance spectra were taken with i) no IDE chip installed (open) and ii) a copper platelet instead of the IDE chip installed (short). With regard to Figure 2 A), these measurements suggested a cable resistance of 0.1 Ohm ($R_{P,1}$), a cable inductance of 80 nH ($L_{P,1}$) and a stray capacitance of 1.0 pF ($C_{Geo,P,1}$). The Bode representation of the open and short spectra are discussed in S4.

3.5 Impedance Data Evaluation to Obtain $\varepsilon_{r,SUT}$ and κ_{SUT}

Within the scope of equivalent circuit analysis of the recorded spectra, $\boldsymbol{Z_M}$ and $\boldsymbol{Z_{SUT}}$ are differentiated by

$$\boldsymbol{Z_M} = \boldsymbol{R_P} + j\omega\boldsymbol{L_P} + \left(\boldsymbol{Z_{SUT}}^{-1} + \left(j\omega\boldsymbol{C_{Geo,P}}\right)^{-1}\right)^{-1} \quad (4)$$

In equation (4), ω and $\boldsymbol{j}$ represent the angular frequency and imaginary unit respectively. With regard to Figure 2 the individual parasitic circuit parameters in equation (4) are assumed equal to $\boldsymbol{R_P} = \boldsymbol{R_{P,1}} + \boldsymbol{R_{P,2}}$, $\boldsymbol{L_P} = \boldsymbol{L_{P,1}} + \boldsymbol{L_{P,2}}$ and $\boldsymbol{C_{Geo,P}} = \boldsymbol{C_{Geo,P1}} + \boldsymbol{C_{Geo,P2}}$.

The measurement conditions for the dielectric reference media used as SUTs 1–6 were carefully chosen to prevent any significant interfacial contributions to $\boldsymbol{Z_{SUT}}$ within the recorded frequency range. Accordingly, the $\boldsymbol{CPE_{DL}}$ circuit element was not included to the data analysis. Owing to the simplicity of the resulting circuit models in Figure 3 II) and III), $\boldsymbol{C_{Geo,SUT}}$ could be explicitly computed for every frequency point recorded. A subsequent frequency averaging step provided a mean value together with a standard uncertainty for $\boldsymbol{C_{Geo,SUT}}$ which was then applied to equation (2) to obtain the respective $\varepsilon_{r,SUT}$ values.

The impedance data collected for the conductivity reference media used as SUTs 7 and 8 was analysed with the circuit model shown in Figure 3 I). The model ensured active compensation of interfacial contributions to $\boldsymbol{Z_{SUT}}$ through the use of the $\boldsymbol{CPE_{DL}}$ circuit component. Best fit estimates of the individual circuit parameters to the experimental data were obtained with the help of the Gamry Echem Analyst software. An estimation of the variance-covariance matrix during the data fit provided standard uncertainties of the respective model parameters. The κ_{SUT} values were computed by applying the estimated $\boldsymbol{R_{S,SUT}}$ to equation (3).

Deviations of $\boldsymbol{C_{Geo,SUT}}$ and $\boldsymbol{R_{S,SUT}}$ derived from triplicate measurements of the same SUT were insignificant in comparison to the uncertainties related to the complete spectrum analysis and thus neglected. The propagation of uncertainty throughout this work was accounted for with the Monte Carlo method through random sampling from normally distributed, uncorrelated input parameters. The corresponding sampling size was set to 10^6. Uncertainties are provided at the coverage factor $\boldsymbol{k}=2$, roughly equivalent to 95 % confidence level.

3.6 Assessment of Accuracy

To evaluate the accuracy of value extraction for $\varepsilon_{r,SUT}$ and $\kappa_{S,SUT}$ from the impedance data, we computed statistically anticipated value ranges based on reference data. For the pure dielectric reference liquids (SUTs 2–4) we used the extensive data published by Gregory and Clark [26]. In their study Gregory and Clark used a shielded two terminal cell with parallel plate geometry which allowed a direct measurement of the static permittivity [18]. Petong, Pottel and Kaatze [31] specified static permittivity values

for ethanol-water mixtures obtained through extrapolation of impedance data recorded with a cut off type reflection cell [32], which were used as a reference for SUTs 5 and 6. The permittivity of nitrogen was not expected to be distinguishable from that of vacuum within the precision of our hardware and the expected $\varepsilon_{r,SUT}$ accordingly set to 1.0 with no uncertainty attached [33]. For the conductivity reference media used as SUTs 7 and 8, κ_{SUT} could be compared to the temperature dependent electrolytic conductivity values specified for the standard solutions. Since the impedance spectra were recorded at a temperature of 21.0 °C we first calculated a reference value at the measurement temperature through linear interpolation of the corresponding values stated at 20 and 25 °C in the literature source. In addition, an expanded uncertainty of the reference value was calculated accounting for (i) the standard uncertainty of the reference values as stated in the literature source, (ii) the temperature uncertainty specified in the literature source and (iii) the temperature uncertainty of this measurement estimated at ±0.5 °C. The individual input values are comprehensively listed in S6.

3.7 Iterative Approach to Determine K_C, $C_{Geo,P}$, R_P and L_P

At the beginning of the data analysis, neither the individual parasitic components $\boldsymbol{R_P}$, $\boldsymbol{C_{Geo,P}}$ and $\boldsymbol{L_P}$ to differentiate between $\boldsymbol{Z_M}$ and $\boldsymbol{Z_{SUT}}$ in equation (4) nor $\boldsymbol{K_C}$ for interpreting $\boldsymbol{C_{Geo,SUT}}$ and $\boldsymbol{R_{S,SUT}}$ in equations (2) and (3) are known. While the impedance contribution of $\boldsymbol{L_P}$ is unique and thus can be easily identified in $\boldsymbol{Z_M}$, the remaining three parameters $\boldsymbol{R_P}$, $\boldsymbol{C_{Geo,P}}$ and $\boldsymbol{K_C}$ can only be determined in a combined approach. The reason is that $\boldsymbol{R_P}$ acts in series with $\boldsymbol{R_{S,SUT}}$ whereas $\boldsymbol{C_{Geo,P}}$ acts in parallel to $\boldsymbol{C_{Geo,SUT}}$. In general, a single equivalent circuit fit to the impedance data can therefore only ascertain the effective sum of $\boldsymbol{R_P}$ with $\boldsymbol{R_{S,SUT}}$ and likewise only the effective sum of $\boldsymbol{C_{Geo,P}}$ and $\boldsymbol{C_{Geo,SUT}}$.

For this purpose, we employed an iterative approach to simultaneously pinpoint $\boldsymbol{R_P}$, $\boldsymbol{C_{Geo,P}}$ and $\boldsymbol{K_C}$ through appropriation of the recorded impedance data of SUTs 1, 3 and 9. As a starting point of the iteration process we use the recorded impedance response of the saturated KCl solution (SUT 9) and hypothesize the resistive current flowing through the setup to be limited by the cabling resistance $\boldsymbol{R_P}$ only. As a consequence, any bulk contributions to $\boldsymbol{Z_{SUT}}$ are, for the initial step, considered negligible, thus leading to the simple $\boldsymbol{Z_{SUT}}$ circuit model in Figure 3 IV). Numerical analysis of the impedance data of SUT 9 with the help of the Echem Analyst software therefore discloses $\boldsymbol{L_P}$ as well as an initial estimate for $\boldsymbol{R_P}$. In the next step, the recorded $\boldsymbol{Z_M}$ of SUTs 1 and 3 are compensated for $\boldsymbol{L_P}$ and $\boldsymbol{R_P}$ to gain unobstructed access to the effective sum of $\boldsymbol{C_{Geo,P}}$ and $\boldsymbol{C_{Geo,SUT}}$.

$$\boldsymbol{C_{Geo}} = \boldsymbol{C_{Geo,P}} + \boldsymbol{C_{Geo,SUT}} = \boldsymbol{C_{Geo,P}} + \frac{\varepsilon_{r,SUT}\varepsilon_0}{\boldsymbol{K_C}} \quad (5)$$

By applying the computed reference values of $\varepsilon_{r,SUT}$ for SUT 1 and 3, equation (5) can be solved for $\boldsymbol{C_{Geo,P}}$ and $\boldsymbol{K_C}$. Now that an estimate for $\boldsymbol{K_C}$ is available, the initial hypothesis of $\boldsymbol{R_{S,SUT}}$ being negligible for SUT 9 may be revisited. The electrolytic conductivity κ_{SUT} of SUT 9 was measured separately with a conductivity probe which suggested a value of 330 000 µS/cm. Accordingly, the initial guess for $\boldsymbol{R_P}$ may then be corrected by a theoretical $\boldsymbol{R_{S,SUT}}$ computed with equation (4) and the $\boldsymbol{K_C}$ value of the previous iteration step. The iteration procedure finishes once the incremental change to $\boldsymbol{R_P}$ by the theoretical computed $\boldsymbol{R_{S,SUT}}$ is smaller than the uncertainty at which $\boldsymbol{R_P}$ can be determined from the experimental data of SUT 9.

4 Results and Discussion

4.1 Parasitic Contributions and Cell Constant for both IDE Geometries

Before taking a look at the bulk properties which can be extracted from the impedance responses of the individual SUTs, we will briefly elucidate the determination process and meaning of parasitics and geometry factor $\boldsymbol{K_C}$ for both IDE system.

The impedance response obtained for SUT 9 which serves as the starting point of the iteration procedure is shown in Figure 6 A). Both the 5 and 10 µm IDE geometry provide similar impedance data for the saturated KCl solution. At frequencies exceeding 0.5 MHz the phase angle rises above 0° which is indicative to the inductive effects imparted by $\boldsymbol{L_P}$. By contrast, the impedance data approaches capacitive behaviour at frequencies below 0.5 MHz which we interpret as the formation of the double layer at the interface between electrode/SUT. For both electrode geometries investigated, $\boldsymbol{L_P}$ appears to resonate with $\boldsymbol{CPE_{DL}}$ at around 0.5 MHz i.e., their contributions to the imaginary part of the measured impedance cancel each other out. At frequencies above the resonance of $\boldsymbol{Z_{SUT}}$ and $\boldsymbol{L_P}$, $\boldsymbol{Z_M}$ is quickly dominated by the parasitic contributions imparted by $\boldsymbol{L_P}$. For this reason, the frequency range at which $\boldsymbol{Z_{SUT}}$ resonates with $\boldsymbol{L_P}$ represents a practical limit to the high frequency end for which parasitic contributions to $\boldsymbol{Z_M}$ can be reasonably compensated for. In other words, $\boldsymbol{L_P}$ prevents a meaningful analysis of $\boldsymbol{Z_{SUT}}$ at arbitrarily large frequencies for IDE geometries.

As shown in in Figure 6 A), the impedance response of SUT 9 modelled by a serial connection of $\boldsymbol{R_P}$, $\boldsymbol{L_P}$ and $\boldsymbol{CPE_{DL}}$ provides for an adequate data fit to be used for the initial step of the iteration process. When compensating the recorded $\boldsymbol{Z_M}$ with $\boldsymbol{R_P}$ and $\boldsymbol{L_P}$ for the dielectric reference SUTs 1–6, we can extract the effective geometric capacitance $\boldsymbol{C_{Geo}}$ as shown in Figure 6 B). Even

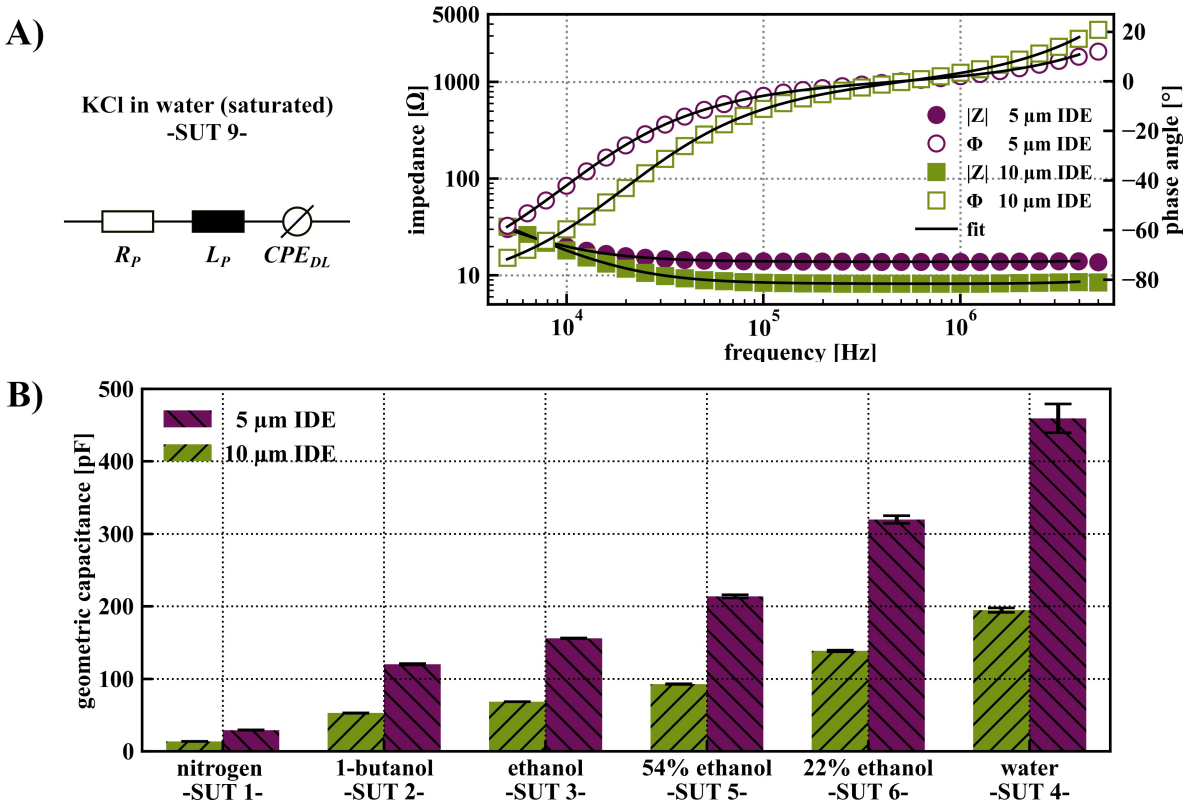

Fig. 6. **A)** Bode representation of the measured impedance spectra obtained from SUT 9 with both the 5 and 10 µm geometry. The simple equivalent circuit model shown next to the graph provides an appropriate fit to the data. Due to the high conductivity of SUT 9, impedance contributions stemming from the geometric capacitance and solution resistance are treated as negligible. The impedance data above 4 MHz appeared unstable and was not included in the data fit. **B)** Total geometric capacitance (parasitic + sample medium) extracted from the impedance spectra of the dielectric SUTs 1–6 recorded with both the 5 and 10 µm electrode geometry. The total geometric capacitance depends strongly on the SUT in contact with the interdigitated area which is an important prerequisite for the relative permittivity determination. The 5 µm electrode used in this study provides a capacitance value consistently 2.2–2.3 times larger than the capacitance obtained from the same SUT when using the 10 µm electrode.

though C_{Geo} contains both parasitic and SUT contributions, we observe a strong dependence of C_{Geo} depending on the sample medium in contact with the interdigitated area. In a previously published IDE study, Rana, Page and McNeil did not observe a substantial difference in C_{Geo} when comparing impedance spectra taken in air and aqueous solutions which was attributed to a disproportionately large $C_{Geo,P}$ [34] Owing to the contrasting results in Figure 6 B) we conclude $C_{Geo,P}$ to be sufficiently minimized allowing for a meaningful analysis of $C_{Geo,SUT}$ in this study.

The actual iteration process to pinpoint R_P, $C_{Geo,P}$, L_P and K_C converges during the first round for the 10 µm and during the second round for the 5 µm IDE. When correcting for the parasitic contributions of the electrical integration of the IDE chip R_{P1}, $C_{Geo,P1}$ and L_{P1} in Figure 2 A), the parasitic contributions imparted by the IDE chips themselves can be estimated and are provided in table 2.

While the $L_{P,2}$ values turn out identical, the parasitic thin film electrode conduction resistance $R_{P,2}$ of the 5 µm IDE compares roughly 70 % larger than of its 10 µm counterpart. A plausible explanation could be a slight variability of the electrode film thickness during the production process which would effectively influence the film resistance between the contact pad and the interdigitated area. However, considering the magnitude of mismatch of $R_{P,2}$ between the two electrode chips investigated, the bottleneck of electron conduction might potentially also be imparted along the electrode fingers itself.

Table 2. Characterization results of the interdigitated electrodes used in this study at $T = 21.0 \pm 0.5$ °C.

parameter	unit	5 µm IDE	10 µm IDE
K_C	m^{-1}	1.68 ± 0.01	3.89 ± 0.02
$R_{P,2}$	Ω	13.7 ± 0.1	8.0 ± 0.1
$L_{P,2}$	nH	30 ± 10	30 ± 10
$C_{Geo,P,2}$	pF	23.1 ± 0.1	10.6 ± 0.1
$\frac{C_{Geo,P,2}K}{\varepsilon_0}$	–	4.4 ± 0.0	4.7 ± 0.0

To substantiate the correlation between $C_{Geo,P2}$ and K_C we applied $C_{Geo,P2}$ and K_C to equation (2) and included the results as the final row in table 2. In both cases we

obtain notably similar permittivity values within the expected range for glasses [35]. This is because the primary contribution to an IDE chip's stray capacitance stems from the electrode substrate the interdigitated structure is deposited on. The slight difference between the 5- and 10-µm value is possibly caused by the neglection of the finite gold film thickness when applying K_C and $C_{Geo,P,2}$ to equation (2).

4.2 Relative Static Permittivity Determination

The static relative permittivity values determined for SUTs 1–6 with equation (3) alongside the expected value ranges are listed in table 3. SUT 1 and 3 are italicized to highlight their appropriation to compute $\boldsymbol{K_C}$ and $\boldsymbol{C_{Geo,P}}$ during the iteration process in the previous chapter. For all SUTs, we observe significant overlap of the frequency averaged relative permittivities extracted from the impedance data recorded between 0.1 and 1 MHz and the anticipated values based on the reference sources for both the 5- and 10-µm electrode.

In the case of deionized water used as SUT 4 however, the computation approach outlined in chapter 3.1 provides a significantly overestimated permittivity value accompanied by a relatively large uncertainty. A likely explanation is the presence of residual conductivities.

While the solution resistance is accounted for in the circuit model, effects related to electrode polarization were deliberately left out as SUTs 1–6 were expected to be sufficiently non-conductive.

Interference of electrode polarization with the measurement however becomes evident when contracting the frequency interval over which the permittivity results are averaged to 0.5–1 MHz as listed in Table 4. By excluding the smaller frequencies, the influence of electrode polarization effects on the static permittivity computation is reduced [18]. Especially the computed values for SUT 4 appear to benefit from the change in computation when comparing the results displayed in table 3 and 4. In general however, we notice two interesting trends.

First, the larger the permittivity of the SUT, the more strongly the measurement appears to be affected by electrode polarization. This observation is not surprising given that the relative permittivity of a solvent is a measure of the solvent molecule's capability to screen the electrostatic interaction of solvated ionic species. The lower the relative permittivity of a solvent, the stronger solvated ionic species interact promoting the occurrence ion association [36]. Associated ions possess no net charge and therefore do not contribute to the electrolytic conductivity of a solvent. For this reason, the high permittivity solvents are more likely to contain fully solvated ionic contaminants imparting an unwanted conductivity thereby shifting electrode polarization related effects to higher frequencies.

The question however is how ionic contaminants are being introduced to the measurement system. A possible answer might be provided when taking a look at the second general trend: The 5-µm electrode is more strongly affected by electrode polarization than the 10-µm electrode. In other words, the measurement with the 5-µm electrode appears to be more strongly affected by ionic contamination than the measurement with the 10-µm electrode. Conversion of the solution resistance parameter which was extracted alongside the geometric capacitance with equation (4) would suggest an electrolytic conductivity for SUT 4 of (5.7±0.3) µS/cm with the 5 µm data and (1.2±0.1) µS/cm with the 10 µm electrode data. As the experiments were carried out in quick succession, an ionic contamination of the sample media stock solutions is ruled out. A slow but steady release of ions from the glass substrate into the SUT above might therefore appear as a plausible explanation. In fact, the ion leaching effect has been identified as the leading contributor to the instability of low conductivity reference standard stored in glass containers [37]. The leaching of ions from the electrode substrate into the liquid phase above would entail a concentration gradient in the liquid phase. As the effective sensing range of the 5 µm IDE structure is half the size of its 10 µm variant, the 5 µm electrode would provide a closer picture of the diffusive boundary layer i.e. detect a greater conductivity. Potentially, the dry etching step used for the electrode preparation might have destabilized the structural integrity of the glass substrate facilitating the leaching of ionic species. From the aspect of ion association, the release of ions from the glass substrate would also provide an explanation to the first general trend. A qualitative assessment regarding the elemental composition of the electrode substrate using energy dispersive X-ray spectroscopy is provided in S7.

Table 3. Static permittivity values obtained through frequency averaging between 0.1 – 1 MHz at $\boldsymbol{T} = 21.0 \pm 0.5\ ^{\circ}\boldsymbol{C}$.

SUT No.	static permittivity		
	5 µm IDE	10 µm IDE	expected range
1	1.0±0.0	1.0±0.0	1.0±0.0
2	18.2±0.2	18.2±0.1	18.1±0.1
3	25.0±0.1	25.0±0.1	25.0±0.1
4	82.6±3.8	80.5±1.4	79.9±0.3
5	36.0±0.4	35.7±0.2	36.3±0.7
6	56.1±1.0	55.8±0.5	55.0±1.1

Table 4. Static permittivity values obtained through frequency averaging between 0.5 – 1 MHz at $\boldsymbol{T} = 21.0 \pm 0.5\ ^{\circ}\boldsymbol{C}$.

SUT No.	static permittivity		
	5 µm IDE	10 µm IDE	expected range
1	*1.0±0.0*	*1.0±0.0*	*1.0±0.0*
2	18.2±0.1	18.2±0.1	18.1±0.1
3	*25.0±0.1*	*25.0±0.1*	*25.0±0.1*
4	80.8±0.8	79.9±0.4	79.9±0.3
5	35.9±0.2	35.7±0.1	36.3±0.7
6	55.6±0.3	55.6±0.2	55.0±1.1

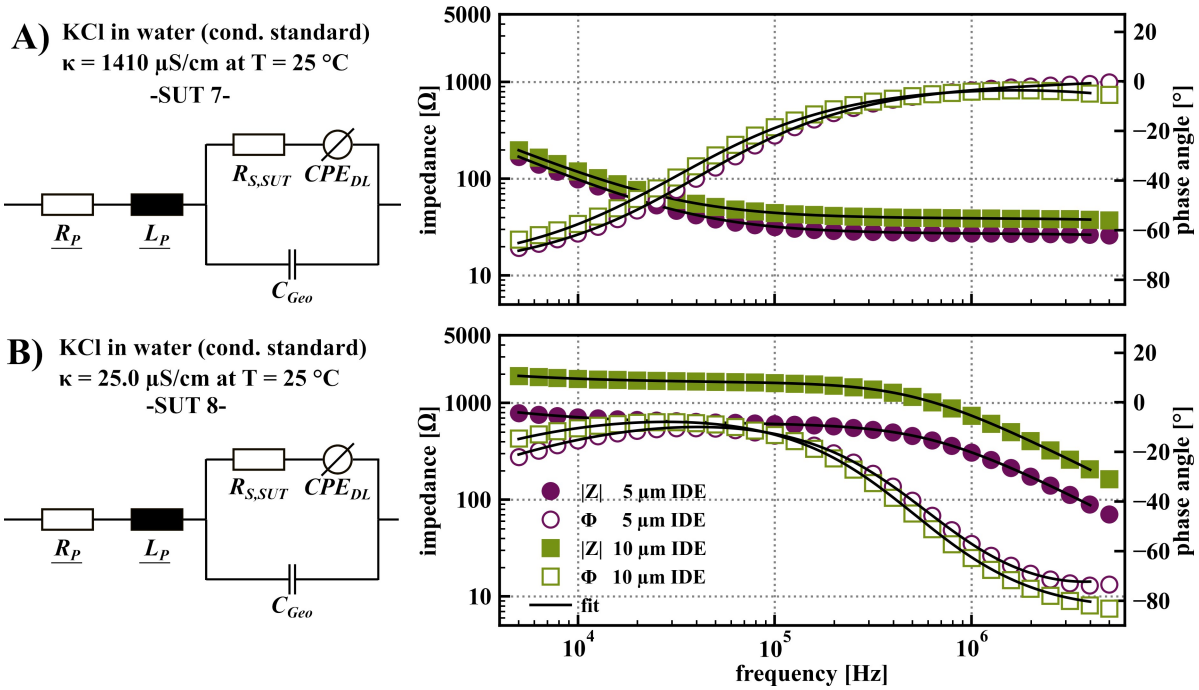

Fig. 7. Bode Plot representation of the measured impedance responses of **A)** SUT 7 and **B)** SUT 8 for both the 5 and 10 µm electrode geometry. The equivalent circuit models are provided alongside the plots. The underlined model parameters were treated as constant during data fit.

4.3 Electrolytic Conductivity Determination

The impedance response of the conductivity reference media used as SUTs 7 and 8 is shown in Figure 7 A) and B) respectively. The equivalent circuit models provided alongside the plots yielded appropriate fits to the measured impedance data for both the 5 and 10 µm IDE geometries. The extracted κ_{SUT} values computed with equation (3) are listed in table 5. Even though the parasitic and interfacial contributions are actively compensated for, κ_{SUT} for SUT 7 is underestimated by up to 3 % for both geometries tested. On the other hand, κ_{SUT} is consistently overestimated for SUT 8. The relative bias between computed and expected κ_{SUT} amounts to up to 8 % for the 10-µm and up to 28 % for the 5 µm geometry. The irregular error structure between expected and computed κ_{SUT} suggests the measurement to be compromised by multiple confounding effects.

Recently, Dizon and Orazem [14a] put forward a system of equations together with practical boundary conditions to model the theoretical impedance response of an interdigitated electrode structure exposed to an electrolyte solution. Their finite element simulation suggested a frequency dispersion of the solution resistance to occur resulting from the nonuniform current and potential distributions.

As a result, the cell constant associated to the electrolytic conductivity was projected to increase by roughly 10 % for a 5 µm IDE as the frequency decreases from f_{CR} to the characteristic frequency associated to the relaxation of solution resistance and double layer capacitance. At f_{CR}, the simulations confirmed equality of the cell constants in equations (3) and (4) for interdigitated electrodes [14a]. The frequency dispersion effect leading to an effective increase of the cell constant might partially explain the underestimation of the electrolytic conductivity value for SUT 7. Interestingly, a slight dependence of K_C on the actual conductivity level is frequently reported for other electrode geometries as well [38].

Regarding the overestimation of the conductivity value for SUT 8 in table 5, the magnitude of deviation between the 5 µm and 10 µm IDE stands out. Similar to what was observed for the high permittivity samples in chapter 4.2, the same SUT analysed with a 5 µm electrode appeared more conductive than when the measurement was taken with the 10 µm electrode. While the conductivity value obtained for SUT 8 with the 10 µm electrode still overestimates the expected value, it is significantly closer to the anticipated value range than the value computed for the 5 µm electrode. Again, it appears plausible that the apparent increase in conductivity may in fact derive

Table 5. Electrolytic conductivity values at $\boldsymbol{T} = 21.0 \pm 0.5\ ^{\circ}\boldsymbol{C}$ extracted from the impedance spectra shown in Figure 7.

SUT No.	electrolytic conductivity [µS/cm]		
	5 µm IDE	10 µm IDE	expected range
7	1270 ± 30	1270 ± 20	1300 ± 10
8	28.6 ± 0.4	24.1 ± 0.3	22.9 ± 0.3

from a potentially slow but steady release of ions from the electrode chip. This assumption is corroborated by the conductivity values obtained for the more conductive SUT 7. For this case, both electrode geometries provide identical conductivity values as the ionic contamination introduced by ion leaching would become negligible in comparison to the native ion content of the SUT.

In addition to the confounding factors outlined thus far, the conductivity values extracted from impedance data are also somewhat subject to the details of how the interfacial contributions are compensated for. For the purpose interfacial compensation, a single constant phase element is used during the data analysis proposed in this study, however expanded models are sometimes found in the literature [14b,38]. Independent of the compensation method applied, interfacial impedance contributions are expected to change over time during prolonged direct exposure of the electrodes to a sample medium [14b] due to e.g. irreversible interfacial reactions or physisorption of dielectric molecules from the sample media to the electrode surface.

5 Conclusion

Interdigitated electrodes are viable sample cells for impedimetric material characterization purposes. Similar to alternative electrode geometries, both parasitic and interfacial contributions to the measured impedance response need to be thoroughly accounted for in order to gain reliable access to the actual bulk impedance contribution exerted by the sample medium under test. In this work, we demonstrated an iterative approach to pinpoint parasitic model parameters as well as the cell constant of an interdigitated structure based on experimental data. Relative static permittivity values extracted from impedance measurements carried out with interdigitated geometries were in excellent agreement with reference values found in the literature. Conductivity values on the other hand proved more challenging to reproduce with the collected impedance data potentially compromised by ionic contamination.

6 Abbreviations

IDE interdigitated electrode
SUT sample medium under test
KCl potassium chloride

7 Symbols

C_{Geo}	total geometric capacitance
$C_{Geo,SUT}$	geometric capacitance imparted by the sample medium under test
$C_{Geo,P}$	parasitic geometric capacitance
$C_{Geo,P,1}$	parasitic geometric capacitance imparted by the electrical connection to the IDE chip
$C_{Geo,P,2}$	parasitic geometric capacitance stemming from the IDE chip itself
CPE_{DL}	constant phase element to model the double layer effect
ε_0	vacuum permittivity
ε_r	relative static permittivity
$\varepsilon_{r,SUT}$	relative static permittivity of the sample medium under test
f_{CR}	characteristic relaxation frequency of κ_{SUT} and $\varepsilon_{r,SUT}$
j	imaginary unit
K_C	cell constant
κ	electrolytic conductivity
κ_{SUT}	electrolytic conductivity of the sample medium under test
L_P	parasitic inductance
$L_{P,1}$	parasitic inductance stemming from the connection to the IDE chip
$L_{P,2}$	parasitic inductance stemming from the IDE chip itself
Φ	phase angle
R_P	parasitic resistance
$R_{P,1}$	parasitic resistance stemming from the connection to the IDE chip
$R_{P,2}$	parasitic resistance stemming from the IDE chip itself
$R_{S,SUT}$	solution resistance of the sample medium under test
T	temperature
ω	angular frequency
$\lvert Z\rvert$	absolute value of the impedance
Z_{IDE}	impedance response of the IDE chip
Z_M	impedance response measured
Z_{SUT}	impedance response of the sample medium under test

8 Supporting Information

Lists of chemicals, equipment, voltages applied as well as the input parameters for the anticipated reference values; open and short measurement without interdigitated chip, and qualitative elemental analysis of the electrode chip.

9 CRediT Authorship Contribution Statement

Benedikt Sapotta: Conceptualization, Methodology, Formal Analysis, Data Curation, Visualization, Software, Investigation, Resources, Writing – Original Draft. Matthias Schwotzer: Visualization, Resources. Matthias Franzreb: Supervision, Project administration Funding acquisition. All authors contributed to the writing - review & editing process.

Acknowledgements

This work was supported by the Deutsche Forschungsgemeinschaft (DFG, German Research Foundation)

under Germany's Excellence Strategy – 2082/1 – 390761711.

Data Availability Statement

The data that support the findings of this study are openly available at https://doi.org/10.17632/txk9gz7gf9.3.

References

[1] A. V. Mamishev, K. Sundara-Rajan, Y. Fumin, D. Yanqing, M. Zahn, *Proc. IEEE* **2004**, *92*, 808–845.

[2] a) L. Bueno, T. R. Paixao, *Talanta* **2011**, *87*, 210–215; b) F. Mohamad, M. A. Sairin, N. N. A. Nizar, S. A. Aziz, D. M. Hazim, S. Misbahulmunir, F. Z. Rokhani, in *Ninth International Conference on Sensing Technology*, **2015**.

[3] A. R. Petre, R. Craciunescu, O. Fratu, *Sensors (Basel)* **2020**, *20*.

[4] a) M. N. Alam, R. H. Bhuiyan, R. A. Dougal, M. Ali, *IEEE Sens. J.* **2010**, *10*, 1243–1248; b) P. Chetpattananondh, K. Thongpull, K. Chetpattananondh, *Computers and Electronics in Agriculture* **2017**, *142*, 545–551.

[5] a) S. Yao, A. Myers, A. Malhotra, F. Lin, A. Bozkurt, J. F. Muth, Y. Zhu, *Adv. Healthcare Mater.* **2017**, *6*; b) S. Ramanathan, M. Jusoh, T. Sabapathy, M. N. Yasin, S. C. B. Gopinath, H. Arahim, M. N. Osman, Y. A. Wahab, *Appl. Phys. A* **2020**, *126*.

[6] a) J. Boudaden, A. Klumpp, I. Eisele, C. Kutter, in *IEEE Sensors*, Orlando, FL, USA, **2016**; b) R. Igreja, C. J. Dias, *Mater. Sci. Forum* **2006**, *514–516*, 1064–1067.

[7] a) I. Kim, A. Rothschild, B. H. Lee, D. Y. Kim, S. M. Jo, H. L. Tuller, *Nano Lett.* **2006**, *6*, 2009–2013; b) F. I. Bohrer, C. N. Colesniuc, J. Park, M. E. Ruidiaz, I. K. Schuller, A. C. Kummel, W. C. Trogler, *J. Am. Chem. Soc.* **2009**, *131*, 478–485; c) I. Musa, G. Raffin, M. Hangouet, M. Martin, A. Alcacer, N. Zine, F. Bellagambi, N. Jaffrezic-Renault, A. Errachid, *Electroanalysis* **2022**.

[8] J. M. Pingarrón, J. Labuda, J. Barek, C. M. A. Brett, M. F. Camões, M. Fojta, D. B. Hibbert, *Pure Appl. Chem.* **2020**, *92*, 641–694.

[9] a) O. O. Soldatkin, I. S. Kucherenko, D. V. Siediuko, D. Y. Kucherenko, S. V. Dzyadevych, A. P. Soldatkin, *Electroanalysis* **2021**, *33*, 2187–2195; b) O. O. Soldatkin, I. S. Kucherenko, V. M. Pyeshkova, A. L. Kukla, N. Jaffrezic-Renault, A. V. El′skaya, S. V. Dzyadevych, A. P. Soldatkin, *Bioelectrochemistry* **2012**, *83*, 25–30.

[10] a) D. Boll, K. Schubert, C. Brauner, W. Lang, *IEEE Sens. J.* **2014**, *14*, 2193–2197; b) M. Kahali Moghaddam, A. Breede, A. Chaloupka, A. Bödecker, C. Habben, E.-M. Meyer, C. Brauner, W. Lang, *Sensors and Actuators A: Physical* **2016**, *243*, 123–133; c) K. G. Bang, J. W. Kwon, D. G. Lee, J. W. Lee, *J. Mater. Process. Technol.* **2001**, *113*, 209–214.

[11] A. Vassilikou-Dova, I. M. Kalogeras, in *Thermal Analysis of Polymers* (Eds.: J. D. Menczel, R. B. Prime), **2009**, pp. 497–613.

[12] M. C. Zaretsky, P. Li, J. R. Melcher, *IEEE Trans. Electr. Insul.* **1989**, *24*, 1159–1166.

[13] B. Sapotta, M. Schwotzer, C. Wöll, M. Franzreb, *Electroanalysis* **2021**.

[14] a) A. Dizon, M. E. Orazem, *Electrochim. Acta* **2019**, *327*; b) A. Dizon, M. E. Orazem, *Electrochim. Acta* **2020**, *337*; c) A. Dizon, C. You, M. E. Orazem, *Electrochim. Acta* **2021**, *391*.

[15] a) C. M. A. Brett, A. M. O. Brett, in *Electrochemistry: Principles, Methods, and Applications*, **1993**, p. 28; b) F. Kremer, A. Schönhals, in *Broadband dielectric spectroscopy* (Eds.: F. Kremer, A. Schönhals), Springer Science & Business Media, **2003**, p. 2.

[16] J. E. Anderson, *J. Non-Cryst. Solids* **1994**, *172–174*, 1190–1194.

[17] U. Kaatze, *Metrologia* **2010**, *47*, S91-S113.

[18] A. P. Gregory, R. N. Clarke, *Meas. Sci. Technol.* **2005**, *16*, 1506–1516.

[19] a) P. Van Gerwen, W. Laureym, W. Laureys, G. Huyberechts, M. Op De Beeck, K. Baert, J. Suls, W. Sansen, P. Jacobs, L. Hermans, R. Mertens, *Sens. Actuators B* **1998**, *49*, 73–80; b) S. Partel, S. Kasemann, V. Matylitskaya, C. Thanner, C. Dincer, G. Urban, *Microelectron. Eng.* **2017**, *173*, 27–32; c) M. Kitsara, D. Goustouridis, S. Chatzandroulis, M. Chatzichristidi, I. Raptis, T. Ganetsos, R. Igreja, C. Dias, *Sens. Actuators B* **2007**, *127*, 186–192.

[20] in *Keysight | Impedance Measurement Handbook, A guide to measurement technology and techniques, 6th Edition - Application Note*, **2020**, pp. 4–01 - 04–25.

[21] H. B. Dwight, *Trans. Am. Inst. Electr. Eng.* **1922**, *41*, 189–198.

[22] E. Barsoukov, R. Macdonald, *Impedance Spectroscopy*, 3 ed., John Wiley & Sons, Inc, **2018**.

[23] C.-u. Kim, G. Li, J. Li, H. Jong, C. Ro, Y. Song, G. Pak, S. Im, *J. Phys. Conf. Ser.* **2013**, *418*.

[24] P. B. Ishai, M. S. Talary, A. Caduff, E. Levy, Y. Feldman, *Meas. Sci. Technol.* **2013**, *24*.

[25] D. He, M. A. Shannon, N. R. Miller, *IEEE Sens. J.* **2005**, *5*, 1185–1196.

[26] A. P. Gregory, R. N. Clark, *NPL Report MAT 23* **2012**.

[27] W. Olthuis, W. Streekstra, P. Bergveld, *Sens. Actuators B* **1995**, *24–25*, 252–256.

[28] B. Timmer, W. Sparreboom, W. Olthuis, P. Bergveld, A. van den Berg, *Lab Chip* **2002**, *2*, 121–124.

[29] K. Nörtemann, J. Hilland, U. Kaatze, *J. Phys. Chem. A* **1997**, *101*, 6864–6869.

[30] F. Kotz, P. Risch, D. Helmer, B. E. Rapp, *Micromachines (Basel)* **2018**, *9*.

[31] P. Petong, R. Pottel, U. Kaatze, *J. Phys. Chem. A* **2000**, *104*, 7420–7428.

[32] O. Göttmann, U. Kaatze, P. Petong, *Meas. Sci. Technol.* **1996**, *7*, 525–534.

[33] L. G. Hector, D. L. Woernley, *Phys. Rev.* **1946**, *69*, 101–105.

[34] S. Rana, R. H. Page, C. J. McNeil, *Electrochim. Acta* **2011**, *56*, 8559–8563.

[35] G. Lüttgens, S. Lüttgens, W. Schubert, in *Static Electricity: Understanding, Controlling, Applying*, Wiley-VCH, Weinheim, Germany, **2017**, p. 79.

[36] M. Yizhak, G. Hefter, *Chem. Rev.* **2006**, *106*, 4585–4621.

[37] R. H. Shreiner, *J. Res. Natl. Inst. Stand. Technol.* **2002**, *107*, 393–399.

[38] C. Thirstrup, L. Deleebeeck, *IEEE Trans. Instrum. Meas.* **2021**, *70*, 1–22.

Received: March 2, 2022
Accepted: May 9, 2022
Published online on ■■, ■■

RESEARCH ARTICLE